chemosensors

MDPI

Article

Machine Learning-Assisted 3D Flexible Organic Transistor for High-Accuracy Metabolites Analysis and Other Clinical Applications

Caizhi Liao [1,2,*], Huaxing Wu [2] and Luigi G. Occhipinti [1,*]

[1] Department of Engineering, The University of Cambridge, Cambridge CB2 1TN, UK
[2] Department of Bioengineering, Sun Yat-Sen University, Guangzhou 510275, China
* Correspondence: cl2006@cam.ac.uk (C.L.); lgo23@cam.ac.uk (L.G.O.)

Abstract: The integration of advanced diagnostic technologies in healthcare is crucial for enhancing the accuracy and efficiency of disease detection and management. This paper presents an innovative approach combining machine learning-assisted 3D flexible fiber-based organic transistor (FOT) sensors for high-accuracy metabolite analysis and potential diagnostic applications. Machine learning algorithms further enhance the analytical capabilities of FOT sensors by effectively processing complex data, identifying patterns, and predicting diagnostic outcomes with 100% high accuracy. We explore the fabrication and operational mechanisms of these transistors, the role of machine learning in metabolite analysis, and their potential clinical applications by analyzing practical human blood samples for hypernatremia syndrome. This synergy not only improves diagnostic precision but also holds potential for the development of personalized diagnostics, tailoring treatments for individual metabolic profiles.

Keywords: machine learning (ML); fiber-based organic transistors (FOTs); metabolic analysis; electrolyte ions; clinical diagnostics

Citation: Liao, C.; Wu, H.; Occhipinti, L.G. Machine Learning-Assisted 3D Flexible Organic Transistor for High-Accuracy Metabolites Analysis and Other Clinical Applications. *Chemosensors* **2024**, *12*, 174. https://doi.org/10.3390/chemosensors12090174

Received: 22 July 2024
Revised: 26 August 2024
Accepted: 28 August 2024
Published: 1 September 2024

1. Introduction

The precise and efficient diagnosis of metabolic disorders is pivotal in clinical medicine, as these conditions often have profound impacts on a patient's overall health and well-being [1–3]. Metabolic ions, such as hydrogen ion (H^+), sodium (Na^+), potassium (K^+), calcium (Ca^{2+}), and magnesium (Mg^{2+}), play critical roles in maintaining cellular function, signal transduction, and homeostasis [4–7]. Imbalances in these ions can indicate the occurrence of various metabolic disorders, including but not limited to, electrolyte imbalances, renal dysfunction, endocrine disorders, and acid–base disturbances. Traditional methods for diagnosing these metabolic ion imbalances often involve a combination of blood tests, urine tests, and sometimes even invasive procedures. However, these methods can be time-consuming, costly, and occasionally lack the sensitivity needed for early detection [8–10].

Recent advancements in technology have led to the development of more sophisticated diagnostic tools that can provide rapid and accurate measurements of metabolic ions. Techniques such as advanced biosensors, mass spectrometry, and ion-selective electrodes are now being integrated into clinical practice [11–13]. These innovations not only improve the speed and accuracy of diagnoses but also enhance the ability to monitor the effectiveness of treatment regimes in real time [14–16]. Tubular and vertical organic transistors are three-dimensional (3D) devices designed to optimize surface area and integration density in flexible electronics. Tubular transistors feature a cylindrical structure, enabling flexibility and stretchability, while vertical transistors stack layers vertically, enhancing current flow and reducing the footprint [17,18]. However, 3D fiber-based organic transistors (FOTs) offer superior attributes, including enhanced mechanical flexibility, greater surface area

for charge transport, and the ability to be woven into fabrics, making them ideal for wearable electronics and other advanced applications where integration with textiles and high mechanical resilience are crucial.

3D flexible FOTs represent a significant innovation in the field of biosensors and bioelectronics, combining the advantages of organic semiconductor materials with the mechanical flexibility necessary for 3D wearable and implantable devices [19–21]. These 3D transistors can be fabricated on flexible fiber substrates, enabling intimate conformal contact with biological fluids and tissues, which is essential for accurate metabolite analysis. The 3D architecture of these devices further enhances their performance by increasing the active surface area, thus improving the sensitivity and accuracy of metabolite detection [22–24].

The incorporation of machine learning (ML) algorithms into the analytical framework of 3D flexible FOTs marks a transformative step forward. Machine learning offers powerful tools for data analysis, capable of handling the complex and high-dimensional data generated by 3D flexible organic transistors [25–27]. Through the application of sophisticated algorithms, ML can discern patterns, predict outcomes, and provide high-accuracy analysis of metabolite levels. This integration of ML not only improves the diagnostic accuracy but also enables the development of personalized medicine by tailoring treatments for individual metabolic profiles [28–31]. Such integrated systems can be particularly beneficial in managing diseases like hypernatremia, where continuous monitoring is crucial. Therefore, the ability to provide rapid and precise metabolite analysis opens new avenues in clinical diagnostics, potentially transforming the landscape of preventive medicine [32–34].

In this work, we report the development of 3D flexible FOT-based sensors supported by ML algorithms and their sensing performance in measuring metabolic electrolyte ions in both artificial solutions and human samples. The 3D flexible FOTs were prepared by coating a multilayered metal/PEDOT:PSS/parylene protective layer onto the nylon fibers. The 3D flexible FOTs working in the depletion mode demonstrate exceptional electrical performances with an ON/OFF ratio of over 1000, excellent bending stability, and robust sensing performance to a range of mostly investigated metabolic ions. By integrating with assorted ML algorithms, the 3D flexible FOT device could accurately evaluate the levels of different metabolic ions, including hydrogen, potassium, sodium, calcium, and magnesium, with a broad range of linear responses. We then tested with practical human blood samples for the clinical diagnosis of hypernatremia syndrome. Results match well with those obtained with the selected benchmark diagnostic approaches. This work envisions ML-assisted 3D flexible FOTs as a promising platform for the accurate diagnosis and monitoring of metabolic ions in practical clinical settings.

2. Materials and Devices

2.1. Materials

Monofilament nylon fibers (Ø 0.50 mm) were purchased from Nantong NTEC monofilament technology Co., Ltd., Nantong, China. Poly(3,4-ethylene dioxythiophene): poly(styrene sulfonate) (PEDOT:PSS) aqueous dispersion (Clevios™ PH 1000) was provided by Heraeus Group, Hanau, Germany. Phosphate-buffered saline (PBS) solution (Gibco™, pH 7.4, 10×) was purchased from Thermo Fisher Scientific, Waltham, MA, USA. Hydrochloric acid (HCl), sodium chloride (NaCl), potassium chloride (KCl), calcium chloride ($CaCl_2$), magnesium sulfate ($MgSO_4$), aluminum sulfate ($Al_2(SO_4)_3$) aqueous solutions were all provided by Sigma-Aldrich Co., St. Louis, MO, USA.

Freshly prepared solutions were used throughout this work. The 10× PBS solution was diluted 10 times with deionized (DI) water, followed by an adjustment of the pH to a value of 7 to produce 1× PBS solution. pH solutions (pH 3.5 to pH 6.0) were prepared by adding a calculated amount of HCl into 1X PBS solution. Similarly, Na^+ solutions (10^{-4} M to 10^0 M), K^+ solutions (10^{-5} M to 10^{-1} M), Ca^{2+} solutions (10^{-6} M to 10^{-2} M), and Mg^{2+} solutions (10^{-5} M to 10^{-1} M) were prepared alike.

The study protocol adhered to the ethical guidelines set forth by the Declaration of Helsinki and received approval from the ethical committee of the Shenzhen People's Hospital (the Second Clinical Medical School affiliated with Jinan University). Written informed consent was obtained from all participants prior to enrollment. Human blood samples were obtained under the approved institutional review board guidelines of the Shenzhen People's Hospital. A sodium blood test is a routine test to check hypernatremia. Blood samples were collected from a vein in the subjects' arms, including both healthy individuals and those diagnosed with hypernatremia. Prior to sample collection, a tourniquet was applied to the upper arm to engorge the veins, and the skin at the insertion site was thoroughly cleaned. A small volume of blood (5 mL) was drawn into a collection tube from each subject. The collected samples were immediately frozen at −80 °C for storage until further analysis. Sodium ion concentrations in the blood samples were subsequently measured using the sodium ion-selective electrode method.

2.2. Device Fabrication

Before the FOT device fabrication, the 3D monofilament nylon fibers were processed with 2 min oxygen plasma (PE-25 Plasma Cleaner, lower power mode) to clean the curved fiber surface. Patterned fiber-shaped source and drain electrodes were fabricated by RF magnetron sputtering (PVD Products, Wilmington, MA, USA) of thin-film layers of chromium (Cr, ~20 nm)/platinum (Pt, ~150 nm) onto a nylon fiber. In the chamber, the fiber was hung on above the sample holder during sputtering to achieve a uniform coating of electrode materials around the curved fiber surface. The width of the channel was controlled to be 0.5 mm by covering laser-cut tape strips (0.5 mm in width) in sputtering and peeling off when finished. A wider laser-cut tape strip (1 mm in width) was then used to define the PEDOT:PSS coating region.

Before dip-coating the PEDOT:PSS active layer, the 3D fiber-shaped source–drain electrode covered with the wider laser-cut tape strip mask was treated with oxygen plasma for 2 min. To improve the conductivity of the channel, dimethyl sulfoxide (DMSO, v/v 5%) and glycerin (v/v 5%) were added into the PEDOT:PSS dispersion and mixed thoroughly. Then the channel region was immersed into the PEDOT:PSS solution, pulled out at a uniform speed (1 cm/min), and dried naturally for 30 min. This same dip-coating process was repeated 5 times to achieve a 3D circular-shaped PEDOT:PSS channel film (~200 nm thick). When the channel region of the fiber source–drain electrode was coated with PEDOT:PSS layer, this device unit was transferred into a glove box filled with high-purity nitrogen gas for post-annealing treatment to optimize the conducting film morphology (100 °C, 1 h) [35]. Next, the encapsulation Parylene out-layer (~2 μm, without covering the channel region) was coated onto the patterned source–drain electrodes using the SCS Labcoter® 3 Parylene Deposition System (Specialty Coating Systems, Indianapolis, IN, USA). Adopting a similar fabrication scheme, raw fiber-shaped gate electrodes (Cr ~20 nm/Pt ~150 nm) were prepared, with an effective gate length of ~5 mm. The tip of the gate electrode could be further modified for different types of chemical and biological sensing applications.

2.3. Device Characterization

Resistance measurements of fiber-shaped electrodes were carried out using a two-probe measurement setup (FLUKE 17B, Everett, WA, USA). The surface of the fiber electrodes was observed with an optical microscope (Leica DM2500, Leica, Wetzlar, Germany). The PEDOT:PSS layer coated on the channel region was characterized by scanning electron microscopy (SEM, JEOL SM-7800F Prime, JEOL, Tokyo, Japan). For this work, over 100 transistor devices were prepared; the device fabrication yield is over 90%. The successfully prepared fiber transistor devices (≈90 transistor devices) were then characterized and measured. These presented results are from the representative devices instead of the best-performing devices.

As a three-terminal sensing system, the 3D flexible FOT sensing device was connected to a measurement unit with two Keithley 4200A-SCS Parameter Analyzer source meters

(Tektronix, Beaverton, OR, USA): the source and drain fabric electrode unit was electrically connected with a source meter, and the raw/modified gate fabric electrode was connected to the other source meter. Two currents, the source–drain current (I_{DS}), flowing through the PEDOT:PSS channel, and the gate current (I_G), flowing through the electrolyte liquid, are induced by two respective voltages, the drain-source voltage (V_{DS}) applied on the channel and the gate voltage (V_G) applied on the gate.

For transfer characteristics, the channel current (I_{DS}) was recorded as a function of V_G (0 to 1.2 V) at a fixed V_{DS} (0.03 V). To enable real-time monitoring of the I_{DS} in fiber-shaped organic electrochemical transistor (OECT)-based sensors exposed to a mixture of various analytes in electrolyte solutions, the device was immersed in the solution under magnetic stirring. This approach is intended to ensure a homogeneous distribution of the analytes within the solution, facilitating consistent interaction with the sensor. V_{DS} was set at 0.03 V, and V_G was set at 0.6 V. In examining the blood sodium ion levels, the classical sodium ion selective electrode method was used as the benchmark clinical approach, and its results were compared with our 3D flexible FOT-generated outputs.

3. Results and Discussion

3.1. Working Principle of 3D Flexible FOTs Sensor

Figure 1a schematically shows the 3D flexible FOT sensor connected to the source meters. In measurement, the application of V_{DS} induces a drift of the holes along the PEDOT:PSS backbone, generating the channel current I_{DS}. The PEDOT:PSS channel current is determined by the de-doping/doping process according to Equation (1) [36,37].

$$n(PEDOT^+ : PSS^-) + M^{n+} + ne^- \underset{Oxidatioin/Doping}{\overset{Reduction/\text{De-doping}}{\rightleftharpoons}} nPEDOT^0 + M^{n+} : nPSS^- \quad (1)$$

Upon the application of a positive V_G, the cations (M^+) from the electrolyte enter the PEDOT:PSS film. These cations penetrate the polymer matrix and interact with the PSS^- polyanion. This interaction results in the de-doping of PEDOT, which decreases its conductivity and modulates the drain current (I_{DS}). While for the doping process, the V_G is removed, M^+ diffuses back into the electrolyte, and $PEDOT^0$ recovers to an oxidized state, generating an increased I_{DS}.

Therefore, the channel current I_{DS} of the fabric organic transistor could be expressed as a function of V_G [38,39], calculated as follows:

$$I_{DS} = \frac{q\mu p_0 tW}{LV_p}\left(V_p - V_G^{eff} + \frac{V_{DS}}{2}\right)V_{DS}, |V_{DS}| \ll \left|V_p - V_G^{eff}\right|;$$

$$V_p = \frac{qp_0 t}{c_i}; \quad (2)$$

$$V_G^{eff} = V_G + V_{offset};$$

where q is the electron charge; μ is the hole mobility; p_0 is the initial hole density of PEDOT:PSS channel; t is the thickness of the PEDOT:PSS layer; W and L represent the width and length of the active channel region, respectively; V_p is the pinch-off voltage; V_G^{eff} is the effective gate voltage applied on the transistor; V_{offset} is the offset voltage at the interfaces; and c_i is the effective gate capacitance per unit area of the transistor. Note that c_i is determined by two interface capacitances: the capacitance of the interface between the electrolyte and PEDOT:PSS channel layer ($C_{E\text{-}C}$) and the capacitance of the interface between the electrolyte and the gate electrode ($C_{G\text{-}E}$) [40], as depicted in Figure 1b. For this work, c_i is assumed to be approximately equal to the sum of the two interface capacitances connected in series divided by the area of the active channel. The coated parylene layers are crucial for their performance and durability. The parylene layer serves as an insulating barrier, preventing electrical short circuits and protecting the underlying organic materials

from moisture and other environmental factors; on the other hand, the parylene layer acts as an encapsulation layer. It provides additional protection from mechanical damage and environmental degradation, thus enhancing the overall longevity and reliability of the device.

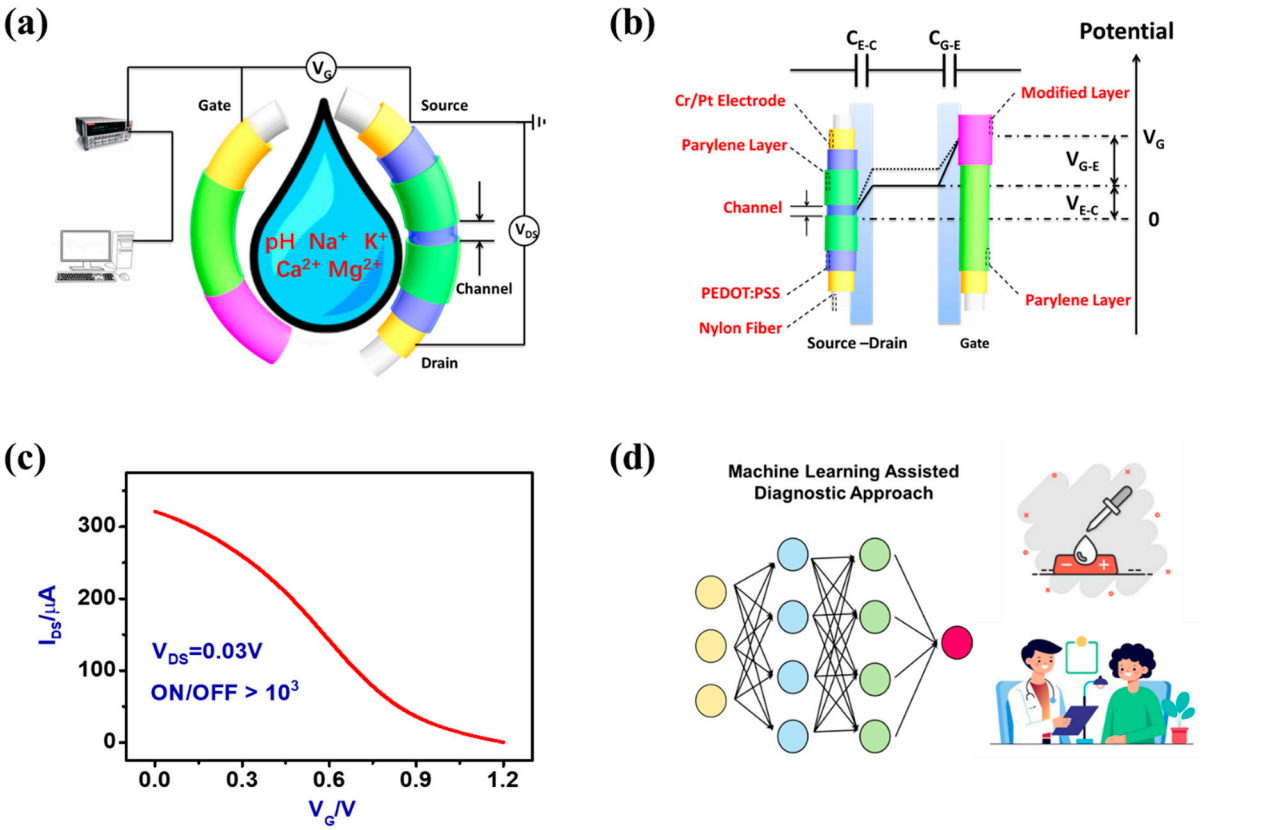

Figure 1. (**a**) Schematic configuration of the 3D flexible FOTs sensing devices as a wearable platform for the measurement of different metabolic ions. (**b**) Schematic figure of the two interfacial potential drops of the 3D flexible FOTs sensing devices operated in the electrolyte. The capacitance of the interface between the electrolyte and PEDOT:PSS channel layer (CE-C: ~0.18 F/cm^2) and the capacitance of the interface between the electrolyte and the gate electrode (CG-E: ~0.23 F/cm^2) are connected in series. Modified layer material: Nafion. (**c**) Transfer characteristics of a 3D flexible FOT sensing device measured at VDS = 0.03 V. (**d**) The ML component improves the device's accuracy and responsiveness by analyzing complex data patterns, which is essential for clinical settings where precise diagnostic capabilities are crucial. By leveraging the combination of flexible materials and intelligent data processing, these FOT devices offer significant potential for non-invasive, real-time monitoring and diagnosis in healthcare.

Interestingly, the 3D flexible FOT sensing device works in a de-doping mode whereby, when a positive VG is applied, improved electrical performance is achieved. In Figure 1c (also in Figure 2c), the ON/OFF ratio was calculated by using the following equation: ON/OFF ratio = ION (~320 μA)/IOFF (~0.2 μA) > 103. From the figures, the ON/OFF current ration is >103 with a gate leakage current lower than 10 nA. Assisted with machine learning algorithms, these 3D flexible FOTs can be used for accurate analysis of different metabolic ion concentrations toward practical clinical diagnoses (Figure 1d).

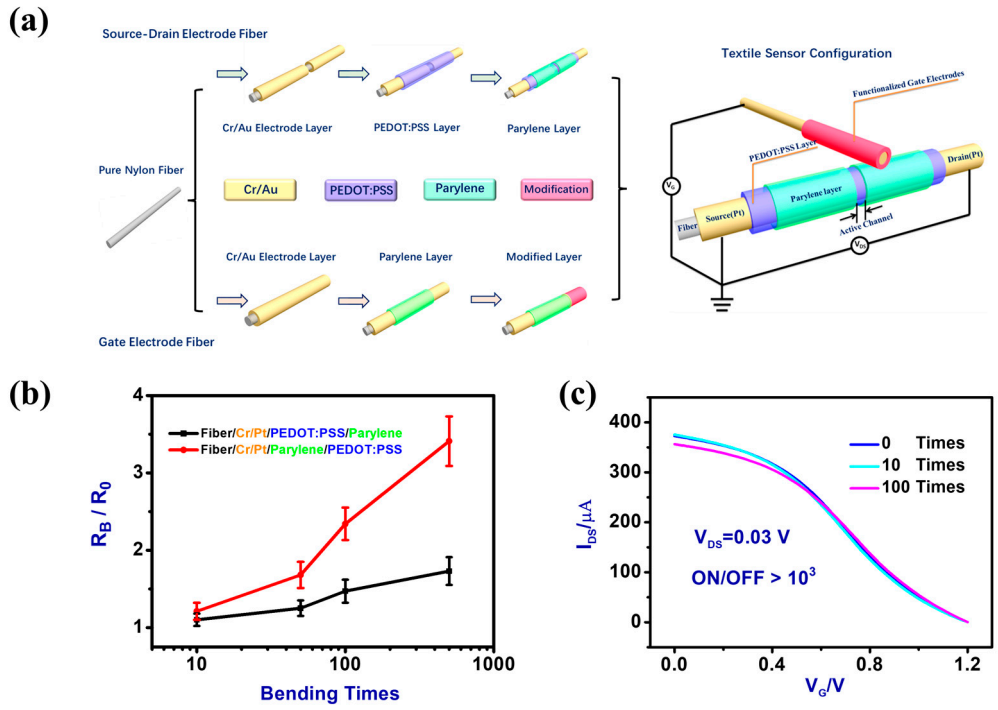

Figure 2. (**a**) The fabrication process of the multilayer fiber-based source–drain electrodes and the bilayer functionalized fiber-based gate electrodes. The paired fiber-shaped OECT devices allow to detect multiple sweat biomarkers. (**b**) Comparative performance study of two types of fiber-based source–drain electrodes (Fiber/Cr/Pt/PEDOT:PSS/Parylene and Fiber/Cr/Pt/Parylene/PEDOT:PSS) before and after repetitive bending. (**c**) Transfer characteristics of a 3D flexible FOT sensing device before and after repetitive bending.

3.2. Optimized Fabrication of 3D Flexible FOT Sensing Devices

A key step to implementing 3D flexible FOT sensing devices is to pair the fabrication process of electric conducting segments with compatible functional components [41]. We reported a straightforward scheme to fabricate 3D fiber-shaped organic transistors with finely defined active channel dimensions (i.e., length and width), which remarkably determine the device performance and the manufacturing reproducibility in a reliable manner [41]. Schematically shown in Figure 2a, the fiber-shaped OECT devices were produced by a multilayered coating procedure. Due to its high electrochemical activity and excellent biocompatibility, Pt was selected as the electrode material [42]. To improve electrode stability, a patterned thin film of Cr as the adhesion layer (~20 nm) was initially sputtered to the oxygen plasma-treated Nylon fibers [43].

For the source–drain 3D fiber electrodes, the bounded raw Cr/Pt film then was coated with a thin layer of PEDOT:PSS (~200 nm thick) using a repeated dip-coating procedure. Finally, a Parylene layer was coated onto the fiber surface except for the active channel region. The results showed that a sequential coating of PEDOT:PSS/Parylene produces a 3D fiber organic transistor with far more bending stability than its counterpart configuration (Parylene/PEDOT:PSS), see Figure 2b. After 500 times bending, the resistance of the Cr/Pt/PEDOT:PSS/Parylene source–drain electrodes increased by less than 50%, while for the Cr/Pt/Parylene/PEDOT:PSS comparative source–drain electrodes, the after-bending resistance is greatly increased by 350%. During bending tests, the Pt film of the original Cr/Pt electrode will be discontinued, generating fractures that prohibit the current flow. Compared to the insulating Parylene layer, the consecutively coated conducting PEDOT:PSS layer will then repair these separated Pt film fractures and help achieve a more stable resistance of the multilayered fiber electrodes. To further study the stability of the fiber electrodes, we recorded the transfer characteristics of the 3D flexible FOT device under bending tests. As shown in Figure 2c, the transfer curve maintains good

electric performance (ON/OFF > 1000) and only slightly shifted even after 100 times bending. Therefore, the simple multilayered structures of Cr/Pt/PEDOT:PSS/Parylene fiber electrodes could be a feasible fabrication strategy for the preparation of highly flexible yet stable 3D FOTs sensor devices. Similarly, the 3D flexible Cr/Pt fiber-shaped gate electrodes were prepared.

3.3. 3D Flexible FOT for Metabolic Ions Analysis

The 3D flexible FOT devices are sensitive to the density of sorted cations in human biological samples which is reflected in the transfer characteristics of the devices, including H^+, Na^+, K^+, Ca^{2+}, and Mg^{2+}. Figure 3a shows the transfer curves (V_{DS} @ 0.03 V) of a 3D flexible FOT device characterized in HCl solutions with different hydrogen concentrations, which corresponded to the pH levels ranging from 3.5 to 6.0 and matched with the slightly acidic human sweat samples (between 4 and 6). The transfer curve shifts to a lower gate voltage with the increase in the concentration of H^+. Therefore, the effective gate voltage would be shifted by the addition of different H^+ concentrations, which could be explained as follows [38]:

$$\begin{aligned} E_{Nerst} &= E^0 + \frac{kT}{ne} \ln Q \\ Q &= \frac{[PEDOT^0]^n [M^{n+}{:}nPSS]}{[PEDOT^+{:}PSS^-]^n [M^{n+}]} \end{aligned} \tag{3}$$

where E^0 is a constant, k is the Boltzmann's constant, T is the temperature, n is the number of transferred electrons, e is the electron charge, and Q is the reaction quotient equilibrium constant. [$PEDOT^0$], [Mn^+: $nPSS^-$], [$PEDOT^+$: PSS^-], and [M^{n+}] are the concentrations of each element in Equation (3), respectively.

For the Equation (3) chemical reaction, the potential applied on the double layer near PEDOT:PSS is given by the Nernst equation above. According to the equivalent circuit for the fiber-shaped OECTs devices coupled with Cr/Pt gate electrode in Figure 1b, the V_G was only partially applied at the interface between the electrolyte and PEDOT:PSS channel film. To compensate for this interface potential shift induced by the cation concentration changes, a higher V_G is needed. Therefore, this fiber transistor device could be calculated with the following:

$$V_g^{eff} = \text{Cons}\tan t + \left(\frac{C_{G-E} + C_{E-C}}{C_{G-E}}\right)\frac{kT}{ne}\ln[M^{n+}] \tag{4}$$

Combined with Equation (2), the magnitude of I_{DS} correlated with the concentration of the cation under a positive V_G was expressed as follows:

$$I_{DS} = \alpha + \beta \ln[M^{n+}] \tag{5}$$

where α is a positive constant and β is a negative constant. As a result, when a positive V_G was applied, the magnitude of the channel's current I_{DS} would be correspondingly reduced with the accumulated level of H^+. According to Equation (2), when V_G is removed, I_{DS} is a constant value referred to as I_0. Therefore, under a positive V_G, the cation de-doping-induced current changes ($|\Delta I|$) can be written as follows:

$$|\Delta I_{M^{n+}}| = |I_{M^{n+}} - I_0| = \alpha^* + \beta^* \ln[M^{n+}] \tag{6}$$

where α^* and β^* are the positive constants. For H^+ concentrations induced responses, $|\Delta I_{Mn+}|$ will linearly increase with the additions of H^+ as per Equation (6) above. Our experimental results further certified that the 3D flexible FOT devices linearly responded to a broad spectrum of H^+ or pH levels (pH 3.5 to pH 6.0, see Figure 3b), which includes the pH physiological range of human biological fluid samples.

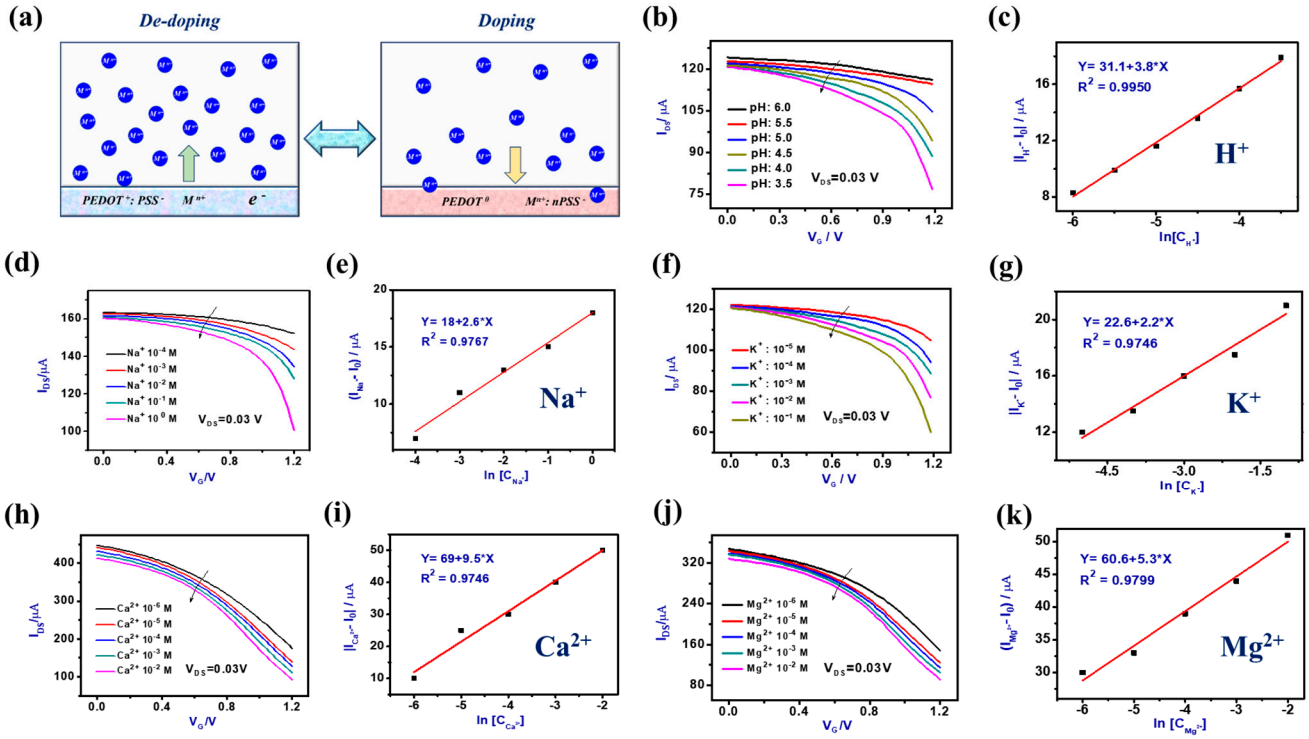

Figure 3. (**a**) Schematic figure of the reversible doping/de-doping process of the 3D flexible FOT devices operated in the electrolyte. (**b**) Transfer characteristics (V_{DS} = 0.03 V) of the 3D flexible FOT device were measured in electrolyte solutions with different concentrations of H^+/pH. (**c**) The current linear response of the 3D flexible FOT device to the H^+ levels ranges from 10^{-6} M to 5×10^{-3} M, with a detection limit down to 10^{-5} M. (**d**) Transfer characteristics (V_{DS} = 0.03 V) of the 3D flexible FOT device were measured in electrolyte solutions with different concentrations of Na^+. (**e**) The current linear response of the 3D flexible FOT device to the Na^+ levels range from 10^{-4} M to 10^{0} M, with a detection limit down to 10^{-3} M. (**f**) Transfer characteristics (V_{DS} = 0.03 V) of the 3D flexible FOT device were measured in electrolyte solutions with different concentrations of K^+. (**g**) The current linear response of the 3D flexible FOT device to the K^+ levels range from 10^{-5} M to 10^{-1} M, with a detection limit down to 10^{-4} M. (**h**) Transfer characteristics (V_{DS} = 0.03 V) of the 3D flexible FOT device were measured in electrolyte solutions with different concentrations of Ca^{2+}. (**i**) The current linear response of the 3D flexible FOT device to the Ca^{2+} levels range from 10^{-6} M to 10^{-2} M, with a detection limit down to 10^{-5} M. (**j**) Transfer characteristics (V_{DS} = 0.03 V) of the 3D flexible FOT device were measured in electrolyte solutions with different concentrations of Mg^{2+}. (**k**) The current linear response of the 3D flexible FOT device to the Mg^{2+} levels range from 10^{-6} M to 10^{-2} M, with a detection limit down to 10^{-5} M.

Working with the same principle, the prepared 3D flexible FOT devices were also used for the analysis of other promising metabolic biomarkers of electrolyte cations in human body fluidic samples, along with Na^+, K^+, Ca^{2+}, and Mg^{2+}. In these FOT sensor devices, the current shifts linearly relative to the additions of assorted cations: $|\Delta I|$ linearly increases with Na^+ in the range of 10^{-4} M to 10^{0} M (Figure 3b,c), K^+ in the range of 10^{-5} M to 10^{-1} M (Figure 3e,f), Ca^{2+} in the range of 10^{-6} M to 10^{-2} M (Figure 3g,h), and Mg^{2+} in the range of 10^{-5} M to 10^{-1} M (Figure 3i,j), with all ranges matching well with the actual concentration range values of the same cations in human biological samples.

3.4. ML-Assisted Metabolic Ions Analysis

An artificial neural network (ANN) comprises interconnected units or nodes known as artificial neurons, with signal processing functionality inspired by the neurons in the human brain (see Figure 4a). Mimicking the brain's synapses, each artificial neuron receives signals from other connected neurons, processes these signals, and then transmits a signal

to other neurons in the network [44]. This signal is represented as a real number, and the neuron's output is calculated using a non-linear function of its input sum, referred to as the activation function. The strength of the signal at each connection is modulated by a weight, which is adjusted during the learning process.

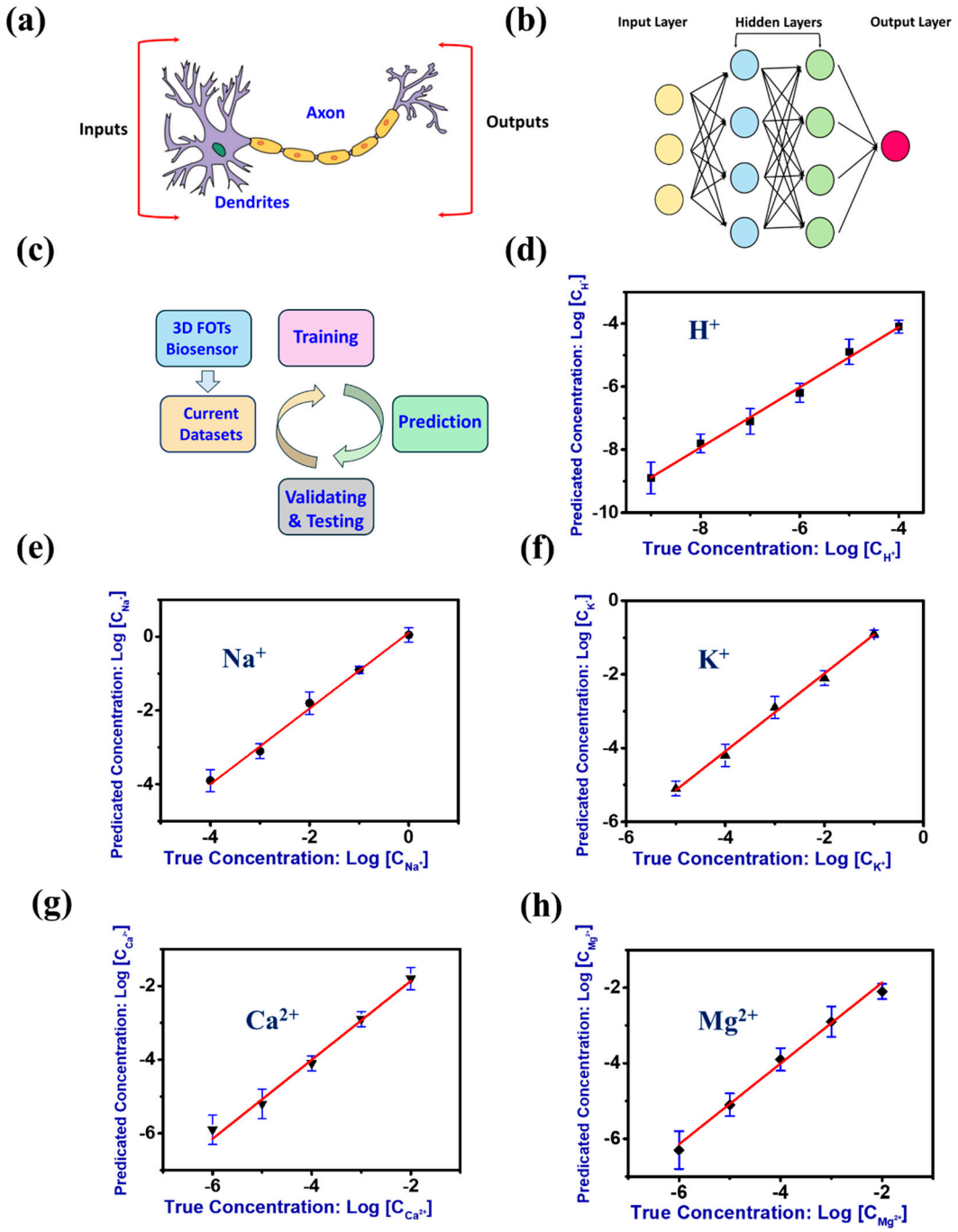

Figure 4. (**a**) A schematical figure of neuron unit in human brain. (**b**) A representative figure of the artificial neuron network model. (**c**) Process flow diagram of the ML-assisted flexible FOTs for metabolic ions analysis. (**d**) Parity plot of true vs. predicted concentrations of H^+ using the ML-assisted flexible FOTs. (**e**) Parity plot of true vs. predicted concentrations of Na^+ using the ML-assisted flexible FOTs. (**f**) Parity plot of true vs. predicted concentrations of Ka^+ using the ML-assisted flexible FOTs. (**g**) Parity plot of true vs. predicted concentrations of Ga^{2+} using the ML-assisted flexible FOTs. (**h**) Parity plot of true vs. predicted concentrations of Mg^{2+} using the ML-assisted flexible FOTs.

Neurons are typically organized into layers, with different layers performing various transformations on their inputs [45,46]. Signals flow from the first layer (input layer) to the final layer (output layer), often through multiple intermediate layers (hidden layers). When a network contains at least two hidden layers, it is commonly termed a deep neural network (see Figure 4b). Artificial neural networks are employed for a wide range of applications, including predictive modeling, adaptive control, and tackling complex problems in artificial intelligence. They have the capability to learn from experience and to draw conclusions from a complex and seemingly unrelated set of data. In this work, ANN is used to model the linear relationship between the concentration of the metabolic analytes and the current value to facilitate the intelligent detection of metabolic ion concentration in real samples.

Several statistical criteria are used to evaluate the effectiveness of modeling methods in accurately detecting metabolic ions. The determination coefficient (R^2) indicates the goodness of fit of the model, with values closer to one signifying a better fit. The root mean square error (RMSE) and mean absolute error (MAE) measure the prediction error of the model, and smaller values are preferred for both. The residual prediction deviation (RPD) assesses the overall prediction capability of the model; an RPD value higher than three indicates excellent predictive performance for analytical purposes [47–49].

As schematically shown in Figure 4c, the flexible FOTs generated current data sets were used for repetitive training, validation, and testing. Assisted with the ANN-based machine learning (ML) algorithms, our flexible FOTs demonstrate excellent accuracy (>99%) toward different metabolic ions analysis (see Figure 4d–h). The ANN models generated parity plots of predicted vs. expected concentration of the different types of metabolic ions (e.g., H^+, Na^+, K^+, Ca^{2+}, and Mg^{2+}) with a superior linear trend ($R^2 > 0.99$) and a broad response range, indicating high prediction capability as supported by the low-resulting RMSE and MAE and high-value RPD (see Table 1). Our research findings highlight the promising potential for synergies between this work and the recent advancements in neuromorphic systems. These synergies could pave the way for innovative approaches that leverage the strengths of both fields, potentially leading to significant breakthroughs in the development of more efficient and intelligent computational models [50]. Therefore, our ML-assisted flexible FOTs hold significant potential for the accurate analysis of metabolic ions in real samples.

Table 1. Performance parameters of deep learning model (ANN)-assisted FOTs detection of metabolic electrolyte ions, including H^+, Na^+, K^+, Ca^{2+}, and Mg^{2+}.

Metabolic Ions	R^2	RMSE	MAE	RPD
H^+	0.9903	0.0806	0.0524	13.6345
Na^+	0.9935	0.0770	0.0441	13.8925
K^+	0.9984	0.0906	0.0755	9.5436
Ca^{2+}	0.9956	0.0893	0.0579	10.4751
Mg^{2+}	0.9947	0.0871	0.0563	12.8942

3.5. ML-Assisted Real Sample Analysis

Hypernatremia is diagnosed when blood sodium levels exceed 145 mmol/L, often due to insufficient water intake or excessive water loss. Symptoms include thirst, confusion, and muscle twitching, with severe cases potentially leading to seizures or coma. Diagnosing hypernatremia involves measuring serum sodium levels through blood tests. As anticipated, our ML-assisted 3D flexible FOTs could accurately detect assorted types of metabolic ions. As a proof-of-concept, we attempted to measure the concentration of Na^+ in the real human blood samples for the diagnosis of hypernatremia cases using our prepared FOT devices. To validate this, we recruited 60 subjects (30 healthy and 30 hypernatremia) and divided them into two groups: a training subjects' group (18 hypernatremia and 18 healthy), whose blood samples were used for the training of our built ML-assisted 3D

flexible FOT system; and testing subjects' group (12 hypernatremia and 12 healthy), whose blood samples were used for the practical testing of hypernatremia, as shown in Figure 5a. During the training session, the gradient descent algorithm is explored through the software of TensorFlow (v2.16.1). Blood samples (≈5 mL) were collected from each subject's vein (lower arm) through a disposable sharp needle and were analyzed by our ML-assisted 3D flexible FOTs (Figure 5b). The testing group data, comprising 12 healthy subjects and 12 hypernatremia cases, were all correctly identified with 100% sensitivity, specificity, and precision (Figure 5c). The ROC curve of the ANN ML-assisted 3D flexible FOTs for clinical diagnostics blood samples of hypernatremia cases were used in Figure 5d. From this ROC curve, our ML-assisted 3D flexible FOTs model performed exceptionally well with the highest accuracy (100%) and AUC (1) in diagnosing real hypernatremia cases. Thus, our proposed system provides a feasible approach for the accurate diagnosis of metabolic disorders caused by the abnormal levels of metabolic ions in human biological samples.

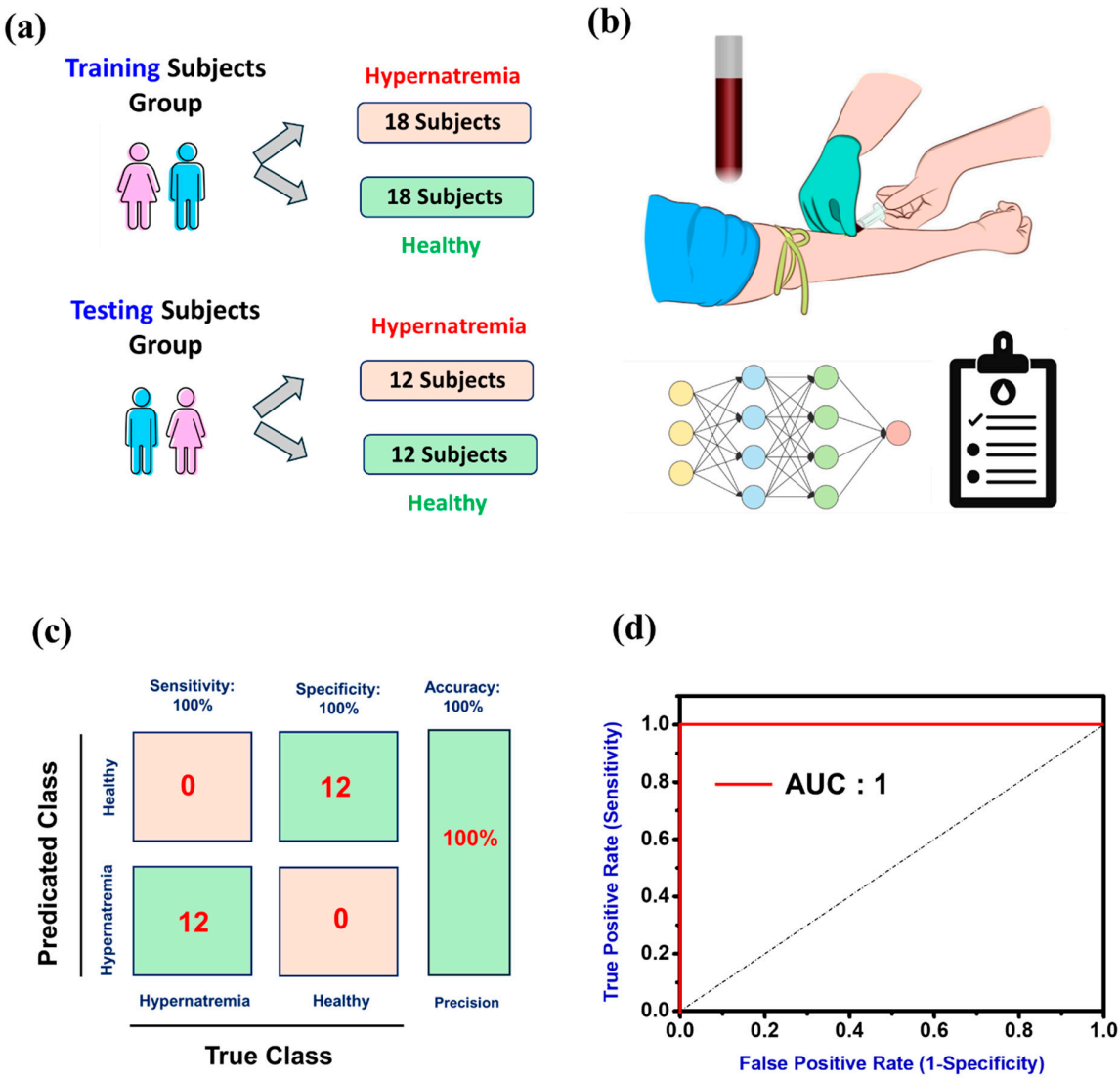

Figure 5. (**a**) A total of 60 recruited subjects are divided into training subjects' group (18 hypernatremia and 18 healthy) and testing subjects' group (12 hypernatremia and 12 healthy). (**b**) Blood samples were collected from a vein in the corresponding subjects' arm, using a small, sharp needle. After the needle was inserted, a small amount (5 mL) of blood was collected in a test tube and stored for further analysis. (**c**) The ML-assisted 3D flexible FOT devices demonstrated 100% accuracy for diagnosing hypernatremia. (**d**) Receiver operating characteristic (ROC) curve of the ANN ML-assisted 3D flexible FOT devices for clinical diagnostics blood samples of hypernatremia subjects.

4. Conclusions

In summary, we developed machine learning-assisted 3D flexible FOT devices for accurate analysis of different types of metabolic ions. The 3D flexible FOTs, constructed by coating multilayered metal, PEDOT:PSS, and protective layers onto Nylon fibers, showcased outstanding electrical performance, including an ON/OFF ratio exceeding 1000, excellent bending stability, and robust sensing capabilities for practical clinical diagnostic applications. Our results suggested that the 3D flexible FOT devices could accurately measure assorted types of sweat electrolyte ions, including H^+, K^+, Na^+, Ca^{2+}, and Mg^{2+}, with a linear response to a broad range of levels, all of which are fully enclosing the normal psychological levels of the corresponding electrolyte ions in human biological samples. By leveraging ANN ML algorithms, these sensors could accurately quantify absolute levels of H^+, K^+, Na^+, Ca^{2+}, and Mg^{2+} with a wide range of linear responses. Clinical testing with human blood samples for hypernatremia diagnosis yielded results that demonstrated 100% accuracy and were consistent with established diagnostic methods. This work highlights the potential of ML-assisted 3D flexible FOTs as a reliable and accurate platform for diagnosing and monitoring metabolic ions in clinical applications. Even though FOTs for sensing metabolic ions offer promising flexibility and miniaturization for wearable and implantable devices, they also face several limitations. Their sensitivity can be compromised by the inherent limitations in fiber material properties and the challenges in achieving uniform ion detection across diverse biological environments. Additionally, maintaining accurate and stable performance in the dynamic and complex biochemical milieu of the body can be difficult. The integration of these sensors into practical devices also involves addressing issues related to biocompatibility, durability, and real-time data accuracy, which are critical for reliable metabolic monitoring.

Supplementary Materials: The following supporting information can be downloaded at: https://www.mdpi.com/article/10.3390/chemosensors12090174/s1, Table S1: Raw measurement data set for the clinical study of hypernatremia diagnosis.

Author Contributions: Conceptualization, C.L. and L.G.O.; Validation, H.W.; Formal analysis, C.L.; Investigation, C.L.; Data curation, H.W.; Writing—original draft, C.L.; Writing—review & editing, H.W. and L.G.O.; Supervision, L.G.O. All authors have read and agreed to the published version of the manuscript.

Funding: This research was funded by the Ministry of Industry and Information Technology (KST202203568423), and EPSRC (grants Nos. EP/K03099X/1, EP/L016087/1, EP/W024284/1, and EP/P027628/1).

Institutional Review Board Statement: The study was conducted in accordance with the Declaration of Helsinki and approved by the Institutional Review Board (or Ethics Committee) of the Shenzhen People Hospital (SZP2022516 and 25 June 2022).

Informed Consent Statement: Informed consent was obtained from all subjects involved in the study.

Data Availability Statement: The original contributions presented in the study are included in the article/Supplementary Material, further inquiries can be directed to the corresponding authors.

Conflicts of Interest: The authors declare no conflicts of interest.

References

1. Rani, V.; Deep, G.; Singh, R.K.; Palle, K.; Yadav, U.C. Oxidative stress and metabolic disorders: Pathogenesis and therapeutic strategies. *Life Sci.* **2016**, *148*, 183–193. [CrossRef] [PubMed]
2. Heindel, J.J.; Blumberg, B.; Cave, M.; Machtinger, R.; Mantovani, A.; Mendez, M.A.; Nadal, A.; Palanza, P.; Panzica, G.; Sargis, R.; et al. Metabolism disrupting chemicals and metabolic disorders. *Reprod. Toxicol.* **2017**, *68*, 3–33. [CrossRef] [PubMed]
3. Hotamisligil, G.S. Inflammation and metabolic disorders. *Nature* **2006**, *444*, 860–867. [CrossRef] [PubMed]
4. Murphy, E.; Steenbergen, C. Ion transport and energetics during cell death and protection. *Physiology* **2008**, *23*, 115–123. [CrossRef]
5. Kolev, S.K.; Petkov, P.S.; Rangelov, M.A.; Trifonov, D.V.; Milenov, T.I.; Vayssilov, G.N. Interaction of Na^+, K^+, Mg^{2+} and Ca^{2+} counter cations with RNA. *Metallomics* **2018**, *10*, 659–678. [CrossRef]

6. Yang, A.; Li, Y.; Yang, C.; Fu, Y.; Wang, N.; Li, L.; Yan, F. Fabric Organic Electrochemical Transistors for Biosensors. *Adv. Mater.* **2018**, *30*, e1800051. [CrossRef]
7. Coppede, N.; Tarabella, G.; Villani, M.; Calestani, D.; Iannotta, S.; Zappettini, A. Human stress monitoring through an organic cotton-fiber biosensor. *J. Mater. Chem. B* **2014**, *2*, 5620–5626. [CrossRef]
8. Mena-Bravo, A.; de Castro, M.D.L. Sweat: A sample with limited present applications and promising future in metabolomics. *J. Pharm. Biomed. Anal.* **2014**, *90*, 139–147. [CrossRef]
9. Roux, A.; Lison, D.; Junot, C.; Heilier, J.F. Applications of liquid chromatography coupled to mass spectrometry-based metabolomics in clinical chemistry and toxicology: A review. *Clin. Biochem.* **2011**, *44*, 119–135. [CrossRef]
10. Dent, A.; Selvaratnam, R. Measuring magnesium—Physiological, Clinical and analytical perspectives. *Clin. Biochem.* **2022**, *105–106*, 1–15. [CrossRef]
11. Ahmed, M.U.; Saaem, I.; Wu, P.C.; Brown, A.S. Personalized diagnostics and biosensors: A review of the biology and technology needed for personalized medicine. *Crit. Rev. Biotechnol.* **2014**, *34*, 180–196. [CrossRef]
12. Crutchfield, C.A.; Thomas, S.N.; Sokoll, L.J.; Chan, D.W. Advances in mass spectrometry-based clinical biomarker discovery. *Clin. Proteom.* **2016**, *13*, 1. [CrossRef] [PubMed]
13. Wang, Y.; Zhou, R.; Cong, H.; Chen, G.; Ma, Y.; Xin, S.; Ge, D.; Qin, Y.; Ramakrishna, S.; Liu, X.; et al. Weak UV-Stimulated Synaptic Transistors Based on Precise Tuning of Gallium-Doped Indium Zinc Oxide Nanofibers. *Adv. Fiber. Mater.* **2023**, *5*, 1919–1933. [CrossRef]
14. Hu, J.; Liu, F.; Chen, Y.; Shangguan, G.; Ju, H. Mass Spectrometric Biosensing: A Powerful Approach for Multiplexed Analysis of Clinical Biomolecules. *ACS Sens.* **2021**, *6*, 3517–3535. [CrossRef] [PubMed]
15. Chiang, C.K.; Chen, W.T.; Chang, H.T. Nanoparticle-based mass spectrometry for the analysis of biomolecules. *Chem. Soc. Rev.* **2011**, *40*, 1269–1281. [CrossRef]
16. Ding, J.; Qin, W. Recent advances in potentiometric biosensors. *TrAC Trends Anal. Chem.* **2020**, *124*, 115803. [CrossRef]
17. Ferro, L.M.M.; Merces, L.; de Camargo, D.H.S.; Bufon, C.C.B. Ultrahigh-Gain Organic Electrochemical Transistor Chemosensors Based on Self-Curled Nanomembranes. *Adv. Mater.* **2021**, *33*, e2101518. [CrossRef]
18. Huang, W.; Chen, J.; Yao, Y.; Zheng, D.; Ji, X.; Feng, L.W.; Moore, D.; Glavin, N.R.; Xie, M.; Chen, Y.; et al. Vertical organic electrochemical transistors for complementary circuits. *Nature* **2023**, *613*, 496–502. [CrossRef]
19. Oluwasanya, P.W.; Carey, T.; Samad, Y.A.; Occhipinti, L.G. Unencapsulated and washable two-dimensional material electronic-textile for NO_2 sensing in ambient air. *Sci. Rep.* **2022**, *12*, 12288. [CrossRef]
20. Choi, H.W.; Shin, D.W.; Yang, J.; Lee, S.; Figueiredo, C.; Sinopoli, S.; Ullrich, K.; Jovancic, P.; Marrani, A.; Momente, R.; et al. Smart textile lighting/display system with multifunctional fibre devices for large scale smart home and IoT applications. *Nat. Commun.* **2022**, *13*, 814. [CrossRef]
21. Lee, S.; Choi, H.W.; Figueiredo, C.L.; Shin, D.-W.; Moncunill, F.M.; Ullrich, K.; Sinopoli, S.; Jovančić, P.; Yang, J.; Lee, H.; et al. Truly form-factor–free industrially scalable system integration for electronic textile architectures with multifunctional fiber devices. *Sci. Adv.* **2023**, *9*, eadf4049. [CrossRef]
22. Baeg, K.J.; Lee, J. Flexible Electronic Systems on Plastic Substrates and Textiles for Smart Wearable Technologies. *Adv. Mater. Technol.* **2020**, *5*, 2000071. [CrossRef]
23. Malik, A.; Kandasubramanian, B. Flexible Polymeric Substrates for Electronic Applications. *Polym. Rev.* **2018**, *58*, 630–667. [CrossRef]
24. Zhang, H.; Wang, Z.; Wang, Z.; He, B.; Chen, M.; Qi, M.; Liu, Y.; Xin, J.; Wei, L. Recent progress of fiber-based transistors: Materials. structures and applications. *Front. Optoelectron.* **2022**, *15*, 2. [CrossRef]
25. Yang, J.; Li, G.; Chen, S.; Su, X.; Xu, D.; Zhai, Y.; Liu, Y.; Hu, G.; Guo, C.; Yang, H.B.; et al. Machine Learning-Assistant Colorimetric Sensor Arrays for Intelligent and Rapid Diagnosis of Urinary Tract Infection. *ACS Sens.* **2024**, *9*, 1945–1956. [CrossRef]
26. Yang, W.; Geng, L. Machine learning assisted electrochemical sensing technology for the detection of nitrate ions in PM2.5. *Int. J. Electrochem. Sci.* **2024**, *19*, 100430. [CrossRef]
27. Tang, M.; Guo, J.; Shen, Z. Rapid detection of carbendazim residue in tea by machine learning assisted electrochemical sensor. *J. Food Meas. Charact.* **2023**, *17*, 6363–6369. [CrossRef]
28. Wang, C.; Hao, T.; Wang, Z.; Lin, H.; Wei, W.; Hu, Y.; Wang, S.; Shi, X.; Guo, Z. Machine learning-assisted cell-imprinted electrochemical impedance sensor for qualitative and quantitative analysis of three bacteria. *Sens. Actuators B Chem.* **2023**, *384*, 133672. [CrossRef]
29. Zhang, J.; Li, C.; Wang, H.; Yang, Z.; Hu, C.; Wu, K.; Hao, J.; Liu, Z. Machine Learning-Assisted Automatically Electrochemical Addressable Cytosensing Arrays for Anticancer Drug Screening. *Anal. Chem.* **2023**, *95*, 18907–18916. [CrossRef] [PubMed]
30. Bao, Q.; Li, G.; Cheng, W.; Yang, Z.; Qu, Z.; Wei, J.; Lin, L. Machine learning-assisted flexible wearable device for tyrosine detection. *RSC Adv.* **2023**, *13*, 23788–23795. [CrossRef]
31. Xu, Y.; Rao, Z.; Liu, Z.; Zheng, W.; Zhou, Y.; Lu, N.; Yang, Y. Improving the Selectivity in Electrochemical Detection of Chloramphenicol Against Metronidazole with Machine Learning. *IEEE Sens. J.* **2023**, *23*, 17883–17890. [CrossRef]
32. Kailasam, V.; Sankararajan, R.; Kailasam, M.; Suseela, S.B. Machine Learning Assisted Metal Oxide-Bismuth Oxy Halide Nanocomposite for Electrochemical Sensing of Heavy Metals in Aqueous Media. *Cryst. Res. Technol.* **2024**, *59*, 2300173. [CrossRef]

33. Wang, B.; Zhang, J.; Wang, T.; Li, W.; Lu, Q.; Sun, H.; Huang, L.; Liang, X.; Liu, F.; Liu, F.; et al. Machine Learning-Assisted Volatile Organic Compound Gas Classification Based on Polarized Mixed-Potential Gas Sensors. *ACS Appl. Mater. Interfaces* **2023**, *15*, 6047–6057. [CrossRef]
34. Aliev, T.A.; Belyaev, V.E.; Pomytkina, A.V.; Nesterov, P.V.; Shityakov, S.; Sadovnichii, R.V.; Novikov, A.S.; Orlova, O.Y.; Masalovich, M.S.; Skorb, E.V. Electrochemical Sensor to Detect Antibiotics in Milk Based on Machine Learning Algorithms. *ACS Appl. Mater. Interfaces* **2023**, *44*, 52010–52020. [CrossRef]
35. Groenendaal, L.; Zotti, G.; Aubert, P.H.; Waybright, S.M.; Reynolds, J.R. Electrochemistry of Poly(3,4-alkylenedioxythiophene) Derivatives. *Adv. Mater.* **2003**, *15*, 855–879. [CrossRef]
36. Liao, C.; Yan, F. Organic Semiconductors in Organic Thin-Film Transistor-Based Chemical and Biological Sensors. *Polym. Rev.* **2013**, *53*, 352–406. [CrossRef]
37. Liao, C.; Mak, C.; Zhang, M.; Chan, H.L.; Yan, F. Flexible organic electrochemical transistors for highly selective enzyme biosensors and used for saliva testing. *Adv. Mater.* **2015**, *27*, 676–681. [CrossRef] [PubMed]
38. Bernards, D.A.; Malliaras, G.G. Steady-State and Transient Behavior of Organic Electrochemical Transistors. *Adv. Funct. Mater.* **2007**, *17*, 3538–3544. [CrossRef]
39. Liao, C.; Zhang, M.; Niu, L.; Zheng, Z.; Yan, F. Highly selective and sensitive glucose sensors based on organic electrochemical transistors with graphene-modified gate electrodes. *J. Mater. Chem. B* **2013**, *1*, 3820–3829. [CrossRef]
40. Millman, J.R.; Bhatt, K.H.; Prevo, B.G.; Velev, O.D. Anisotropic particle synthesis in dielectrophoretically controlled microdroplet reactors. *Nat. Mater.* **2005**, *4*, 98–102. [CrossRef]
41. Maccioni, M.; Orgiu, E.; Cosseddu, P.; Locci, S.; Bonfiglio, A. Towards the textile transistor Assembly and characterization of an organic field effect transistor with a cylindrical geometry. *Appl. Phys. Lett.* **2006**, *89*, 143515. [CrossRef]
42. Qian, X.; Ko, A.; Li, H.; Liao, C. Flexible non-enzymatic glucose strip for direct non-invasive diabetic management. *Microchem. J.* **2024**, *197*, 109818. [CrossRef]
43. Tang, H.; Lin, P.; Chan, H.L.; Yan, F. Highly sensitive dopamine biosensors based on organic electrochemical transistors. *Biosens. Bioelectron.* **2011**, *26*, 4559–4563. [CrossRef]
44. Otchere, D.A.; Ganat, T.O.A.; Gholami, R.; Ridha, S. Application of supervised machine learning paradigms in the prediction of petroleum reservoir properties: Comparative analysis of ANN and SVM models. *J. Pet. Sci. Eng.* **2021**, *200*, 108182. [CrossRef]
45. Bisgin, H.; Bera, T.; Ding, H.; Semey, H.G.; Wu, L.; Liu, Z.; Barnes, A.E.; Langley, D.A.; Pava-Ripoll, M.; Vyas, H.J.; et al. Comparing SVM and ANN based Machine Learning Methods for Species Identification of Food Contaminating Beetles. *Sci. Rep.* **2018**, *8*, 6532. [CrossRef]
46. Roman-Portabales, A.; Lopez-Nores, M.; Pazos-Arias, J.J. Systematic Review of Electricity Demand Forecast Using ANN-Based Machine Learning Algorithms. *Sensors* **2021**, *21*, 4544. [CrossRef] [PubMed]
47. Kumar, A.; Jain, D.; Bahuguna, J.; Bhaiyya, M.; Dubey, S.K.; Javed, A.; Goel, S. Machine learning assisted and smartphone integrated homogeneous electrochemiluminescence biosensor platform for sample to answer detection of various human metabolites. *Biosens. Bioelectron.* **2023**, *238*, 115582. [CrossRef]
48. Ge, Y.; Liu, P.; Chen, Q.; Qu, M.; Xu, L.; Liang, H.; Zhang, X.; Huang, Z.; Wen, Y.; Wang, L. Machine learning-guided the fabrication of nanozyme based on highly-stable violet phosphorene decorated with phosphorus-doped hierarchically porous carbon microsphere for portable intelligent sensing of mycophenolic acid in silage. *Biosens. Bioelectron.* **2023**, *237*, 115454. [CrossRef]
49. Prakasha, B.S.; Shukla, G.; Subramanian, A. Discriminative analysis of volatile organic compounds using machine-learning assisted Au loaded ZnO and TiO_2-based thin film sensors. *Sens. Actuator A Phys.* **2024**, *373*, 115385. [CrossRef]
50. Merces, L.; Ferro, L.M.M.; Nawaz, A.; Sonar, P. Advanced Neuromorphic Applications Enabled by Synaptic Ion-Gating Vertical Transistors. *Adv. Sci.* **2024**, *11*, e2305611. [CrossRef]